PHYSICAL REVIEW C **95**, 064322 (2017)

β-decay half-lives and β-delayed neutron emission probabilities for several isotopes of Au, Hg, Tl, Pb, and Bi, beyond $N = 126$

R. Caballero-Folch,[1,2,*] C. Domingo-Pardo,[3] J. Agramunt,[3] A. Algora,[3,4] F. Ameil,[5] Y. Ayyad,[6] J. Benlliure,[6] M. Bowry,[7] F. Calviño,[1] D. Cano-Ott,[8] G. Cortès,[1] T. Davinson,[9] I. Dillmann,[2,5,10] A. Estrade,[5,11] A. Evdokimov,[5,10] T. Faestermann,[12] F. Farinon,[5] D. Galaviz,[13] A. R. García,[8] H. Geissel,[5,10] W. Gelletly,[7] R. Gernhäuser,[12] M. B. Gómez-Hornillos,[1] C. Guerrero,[14,15] M. Heil,[5] C. Hinke,[12] R. Knöbel,[5] I. Kojouharov,[5] J. Kurcewicz,[5] N. Kurz,[5] Yu. A. Litvinov,[5] L. Maier,[12] J. Marganiec,[16] M. Marta,[5,10] T. Martínez,[8] F. Montes,[17,18] I. Mukha,[5] D. R. Napoli,[19] C. Nociforo,[5] C. Paradela,[6] S. Pietri,[5] Zs. Podolyák,[7] A. Prochazka,[5] S. Rice,[7] A. Riego,[1] B. Rubio,[3] H. Schaffner,[5] Ch. Scheidenberger,[5,10] K. Smith,[5,17,18,20,21] E. Sokol,[22] K. Steiger,[12] B. Sun,[5] J. L. Taín,[3] M. Takechi,[5] D. Testov,[22,23] H. Weick,[5] E. Wilson,[7] J. S. Winfield,[5] R. Wood,[7] P. J. Woods,[9] and A. Yeremin[22]

[1]*INTE, DFEN - Universitat Politècnica de Catalunya, E-08028 Barcelona, Spain*
[2]*TRIUMF, Vancouver, British Columbia V6T 2A3, Canada*
[3]*IFIC, CSIC - Universitat de València, E-46071 València, Spain*
[4]*Institute of Nuclear Research of the Hungarian Academy of Sciences, Debrecen H-4001, Hungary*
[5]*GSI Helmholtzzentrum für Schwerionenforschung GmbH, D-64291 Darmstadt, Germany*
[6]*Universidade de Santiago de Compostela, E-15782 Santiago de Compostela, Spain*
[7]*Department of Physics, University of Surrey, Guildford GU2 7XH, United Kingdom*
[8]*CIEMAT, E-28040 Madrid, Spain*
[9]*University of Edinburgh, Edinburgh EH9 3JZ, United Kingdom*
[10]*Justus-Liebig-Universität Giessen, D-35392 Giessen, Germany*
[11]*St. Mary's University, Halifax, Nova Scotia B3H 3C3, Canada*
[12]*Physik Department E12, Technische Universität München, D-85748 Garching, Germany*
[13]*Centro de Física Nuclear da Universidade de Lisboa, 169-003 Lisboa, Portugal*
[14]*CERN Physics Department, CH-1211 Geneve, Switzerland*
[15]*Universidad de Sevilla, E-41080 Sevilla, Spain*
[16]*ExtreMe Mater Institute, D-64291 Darmstadt, Germany*
[17]*NSCL, Michigan State University, East Lansing, Michigan 48824, USA*
[18]*Joint Institute for Nuclear Astrophysics, Notre Dame, Indiana 46615, USA*
[19]*Instituto Nazionale di Fisica Nucleare, Laboratori Nazionale di Legnaro, I-35020 Legnaro, Italy*
[20]*University of Notre Dame, South Bend, Indiana 46556, USA*
[21]*University of Tennessee, Knoxville, Tennessee 37996, USA*
[22]*Flerov Laboratory, Joint Institute for Nuclear Research, 141980 Dubna, Russia*
[23]*Institute de Physique Nucléaire d'Orsay, F-91405 Orsay, France*

(Received 19 January 2017; published 23 June 2017)

Background: There have been measurements on roughly 230 nuclei that are β-delayed neutron emitters. They range from ^{8}He up to ^{150}La. Apart from ^{210}Tl, with a branching ratio of only 0.007%, no other neutron emitter has been measured beyond $A = 150$. Therefore, new data are needed, particularly in the region of heavy nuclei around $N = 126$, in order to guide theoretical models and help understand the formation of the third r-process peak at $A \sim 195$.
Purpose: To measure both β-decay half-lives and neutron branching ratios of several neutron-rich Au, Hg, Tl, Pb, and Bi isotopes beyond $N = 126$.
Method: Ions of interest were produced by fragmentation of a ^{238}U beam, selected and identified via the GSI-FRS fragment separator. A stack of segmented silicon detectors (SIMBA) was used to measure ion implants and β decays. An array of 30 ^{3}He tubes embedded in a polyethylene matrix (BELEN) was used to detect neutrons with high efficiency and selectivity. A self-triggered digital system is employed to acquire data and to enable time correlations. The latter were analyzed with an analytical model and results for the half-lives and neutron-branching ratios were derived by using the binned maximum-likelihood method.
Results: Twenty new β-decay half-lives are reported for $^{204-206}$Au, $^{208-211}$Hg, $^{211-216}$Tl, $^{215-218}$Pb, and $^{218-220}$Bi, nine of them for the first time. Neutron emission probabilities are reported for ^{210,211}Hg and $^{211-216}$Tl.

*rcaballero-folch@triumf.ca; roger@baeturia.com

Conclusions: The new β-decay half-lives are in good agreement with previous measurements on nuclei in this region. The measured neutron emission probabilities are comparable to or smaller than values predicted by global models such as relativistic Hartree Bogoliubov plus the relativistic quasi-particle random phase approximation (RHB + RQRPA).

DOI: 10.1103/PhysRevC.95.064322

I. INTRODUCTION

Very-neutron-rich nuclei may emit one or more neutrons when they disintegrate via β decay. This is the so-called β-delayed neutron (βn) emission process, which is energetically allowed when the Q_β value of the decay exceeds the neutron separation energy S_n of the daughter nucleus. The βn emission has been experimentally determined for about 230 neutron-rich nuclei, spanning from ^{8}He up to ^{150}La [1–4]. Most of these measurements took advantage of the large fission yields around the two fission peaks at $A \sim 95$ and $A \sim 138$ in thermal neutron-induced fission. However, β-delayed neutron emission has remained essentially inaccessible for nuclei heavier than $A = 150$, where only a minuscule value of 0.007% has been reported for the βn-emission probability of ^{210}Tl [5,6]. Because of the scarce or nonexistent βn data in the heavy-mass region, rapid neutron capture r-process [7] calculations have to rely entirely on theoretical models [8–10]. However, the performance of such models for reproducing the features of the β decay in r-process waiting-point nuclei has been tested with experimental data only for the two shell closures at $N = 50$ and $N = 82$ from measurements such as those reported in Refs. [11–17]. The comparison is much more limited in the $N = 126$ region, where only half-lives in the neighborhood of the doubly magic ^{208}Pb were available (see, e.g., Ref. [18]).

The neutron-rich nuclei "south" of ^{208}Pb are difficult to study experimentally because of the very small production cross sections and the large background induced by the heavy primary beam. In the present work it was possible to produce and identify reliably secondary neutron-rich nuclei in the region "south-east" of ^{208}Pb in the chart of nuclides thanks to the high-energy (1 GeV/u) ^{238}U beams available at the GSI facility. Extended motivation and results for this experiment were recently published in Ref. [19]. Here we present more details on the experimental apparatus in Sec. II, the analysis methodology and results, which are reported in Sec. III and, finally, Secs. IV and V summarize the main results and conclusions.

II. EXPERIMENTAL SETUP AND ION IDENTIFICATION

The present measurements were carried out at the GSI Helmholtz Center for Heavy Ion Research. A ^{238}U beam was accelerated to an energy of 1 GeV/u by the UNILAC linear accelerator coupled to the SIS 18 synchrotron. The average beam intensity was 2×10^9 ions/spill, with a pulsed beam structure of 1 s spill duration (SIS extraction) and a repetition cycle of 4 s. The beam impinged on a ^{9}Be target with a thickness of 1.6 g/cm^2 at the entrance of the fragment separator (FRS) [20]. The selection of the ions of interest, from this point to the detection system, was done with the $B\rho$-ΔE-$B\rho$ method by using the FRS as an achromatic spectrometer. Neutron-rich nuclei "south-east" of ^{208}Pb in the chart of nuclides were produced by using two FRS settings centered on ^{211}Hg and ^{215}Tl. To minimize the number of ionic charge states of the secondary beam a niobium layer with a thickness of 223 mg/cm^2 was placed behind the Be target. In addition, a homogeneous Al degrader with a thickness of 2.5 g/cm^2 was placed at the first FRS focal plane (S1) in combination with thick Cu slits, which served to reduce the contribution of fission fragments and primary beam charge states with magnetic rigidity $B\rho$ initially similar to that of the setting isotope. A wedge-shaped Al degrader with a thickness of 3874 mg/cm^2 was employed as achromatic degrader at the intermediate focal plane S2 (see Fig. 1).

Ion species were identified by means of standard FRS tracking detectors. Two plastic scintillators located at S2 and at the final focal plane S4 were used to measure the time of flight (t_{TOF}) of the ions. Two systems of time projection chambers (TPCs) [21] placed at S4 and S2 allowed us to determine accurate $B\rho$ values for each ion by measuring their trajectory with respect to the central fragment. The measured t_{TOF} in combination with the $B\rho$ provided the necessary information to calculate the mass-to-charge ratio (A/q) on an event-by-event basis. The resolution thus obtained in A/q was 2.5‰ full width at half maximum (FWHM).

To determine the atomic number Z, two fast multiple sampling ionization chambers (MUSICs) [22] were placed in the S4 experimental area. Although the detected nuclei were mainly bare, H- and He-like charge states were also detected in the MUSICs. These events were corrected by combining the information of the two MUSICs and calculating the energy loss in the S2 degrader following the method applied in previous studies in this mass region [23–26]. In addition, it was needed to treat the gain fluctuations in the MUSIC detectors caused by the variations of the temperature in the experimental hall, and consequent changes in gas pressure, which were also corrected numerically [27]. The final resolution obtained in Z for the Pb-Bi region was of $\lesssim$6‰ FWHM. Finally, the Z versus A/q particle identification diagram (PID) was experimentally validated with a dedicated run. ^{205}Bi ions were implanted into a passive plastic stopper and the decays of well-known isomeric transitions [28] were measured with HPGe detectors.

The PID obtained, including nuclei produced in both FRS settings with all the statistics accumulated during the

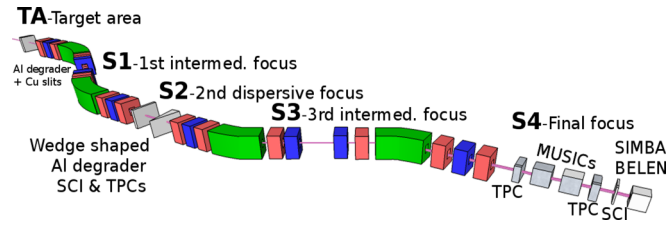

FIG. 1. Scheme of FRS facility (see text for details).

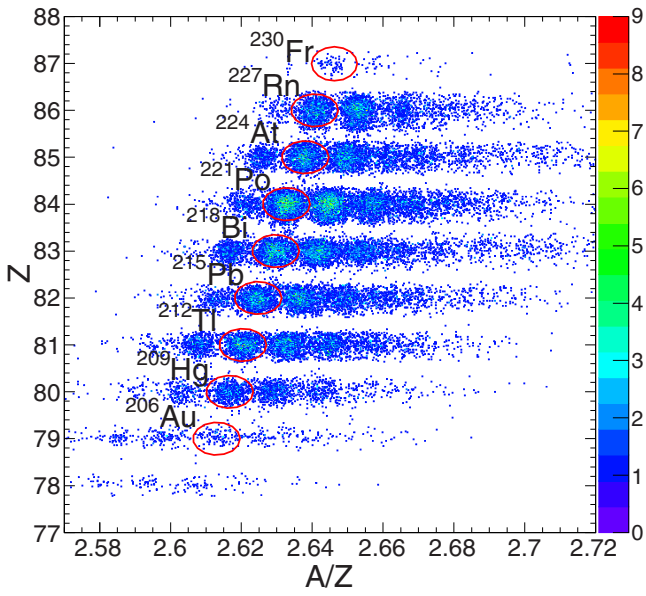

FIG. 2. Particle identification diagram (PID) with the total statistics of the ^{211}Hg and ^{215}Tl settings.

experiment, is shown in Fig. 2. All identified nuclei were already reported in previous experiments [29,30].

A. Implantation and decay-detection system

The secondary beam of neutron-rich isotopes was focused at the final focal plane S4 of the FRS. A third Al degrader with variable thickness was adjusted in order to slow down the ions of interest and to implant them into the central region of an active stopper named "silicon implantation beta absorber" (SIMBA) [31,32]. SIMBA enabled position and energy measurement of heavy charged ions as well as charged particles from α and β decays. The main difference between the SIMBA system employed here and previous versions was the smaller number of Si detectors required to stop and implant the ions in the present experiment, which had a higher atomic number ($Z \sim 82$) than those measured in the past ($Z \sim 50$, [31]). In addition, the geometry and overall size of SIMBA were also modified in order to optimize neutron detection (see below). The present SIMBA version consisted of a stack of nine highly segmented Si detectors (see Figs. 3 and 4).

The first two layers, called XY-tracking detectors, consisted of single-sided Si-strip detectors (SSSDs) with their strips in orthogonal orientation with respect to each other. They were used for determining accurately the ion position in the transversal plane of the beam. A center-of-gravity method applied to the charge shared over all the strips allowed us to determine the ion position with an accuracy of ± 1 mm^2 [27,34], corresponding to one pixel in a silicon layer of SIMBA. The implant and decay-sensitive region consisted of two SSSD layers (front absorbers), three double-sided silicon stripped detectors (DSSSDs) designated as implantation layers A, B, and C, and two SSSD layers (rear absorbers). The energy deposited by the ions along these seven Si detectors was used to detect whether the ion was implanted or if it punched through, as well as to determine the corresponding implant layer or depth. The segmentation of the DSSSDs was 60-fold in the X and 40-fold in the Y direction, with a strip width of 1 mm. Figure 5 shows the total number of implanted ions for each isotope in the DSSSDs of SIMBA.

The energy deposited by β decays in each Si-electrode showed, as expected, a continuum spectrum which extended up to ~2–3 MeV. The energy deposited in the DSSSDs was determined from the response of the Y strips, which were readout via logarithmic preamplifiers. The latter allowed clear separation of the ion implants and decays in the spectrum [see Table I and Figs. 6(a) and 6(b)]. A pulse generator was used to perform the gain-matching of the Y strips. An accurate energy calibration of layers A and B was accomplished using well-known α decays from several At, Bi, Rn, and Po isotopes produced in the decay of implanted Tl, Pb, and Bi nuclei [see Figs. 6(a) and 6(b)]. No α emitter was implanted in layer C and, therefore, a coarse energy calibration of the latter was made by using only the broad β spectrum [Fig. 6(d)]. Nevertheless, for implant-β time correlations only an energy window covering the broad β spectrum is required and, therefore, an accurate energy calibration is of secondary relevance for this data analysis.

SIMBA was placed inside the cylindrical hole (23 cm diameter) of the beta delayed neutron (BELEN) detector [46–49]. BELEN consisted of an array of 30 ^{3}He counters of

FIG. 3. Picture of SIMBA without its cylindrical coverage of 11.5 cm diameter.

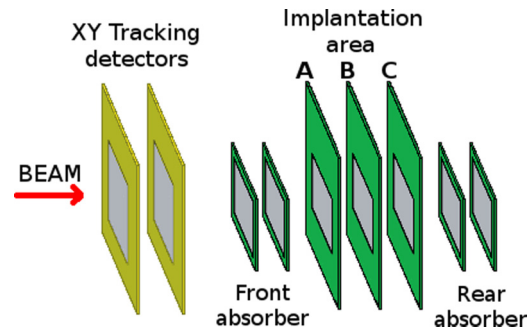

FIG. 4. Schematic view of SIMBA: From left to right (beam direction) the two XY-tracking silicons, the front absorber, the implantation layers A, B, and C and the rear absorber layers. Adapted from Refs. [32,33].

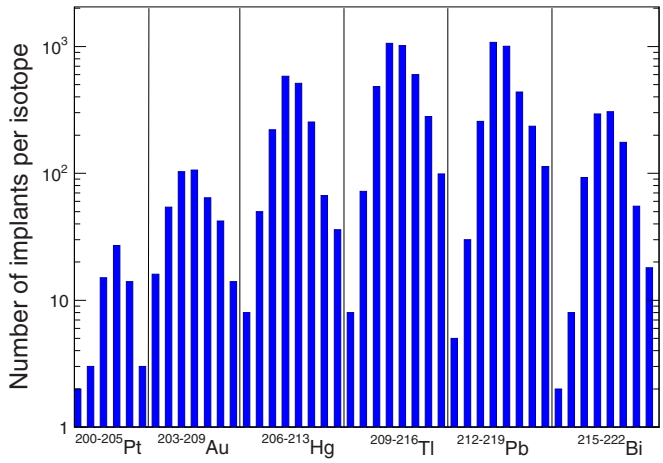

FIG. 5. Number of implanted nuclei of each isotope in the DSSSDs of SIMBA.

2.54 cm diameter, embedded in a high-density polyethylene (PE) matrix (Fig. 7). The ^{3}He tubes were distributed in two rings: an inner one with a radius of 14.5 cm and 10 tubes of 10 atm, and the outer ring with a radius of 18.5 cm and 20 tubes of 20 atm. This configuration was designed by means of GEANT4 [50,51] and MCNPX [52–54] Monte Carlo (MC) simulations in order to achieve a high and flat detection efficiency (see Fig. 8). At a neutron energy up to 1 MeV the detection efficiency was 40(2)%, and it decreased to 25% at 5 MeV. The MC codes were experimentally validated at $E_n = 2.3$ MeV with a dedicated measurement of a well-calibrated ^{252}Cf source.

The $Q_{\beta n}$ window of the exotic nuclei involved in the present measurement spans neutron energies up to 2.5 MeV [55,56]. In this energy range, the average neutron detection efficiency was 38%; this value was used in the data analysis (see Sec. III). By using the calibrated ^{252}Cf source a gain matching of the response of all 30 counters was carried out before the experiment. The stability of the overall detector response was checked regularly during the experiment. The accumulated spectrum for all 30 tubes during the ^{211}Hg setting is shown Fig. 9.

TABLE I. α lines observed in SIMBA in layers A and B and their associated nuclei [see some of them in Figs. 6(b) and 6(c)].

α energy (keV)	SIMBA layer	α emitter	Precursor implanted
5304.3 [35]	A, B	^{210}Po	(Implanted)
5869.5 [36]	A	^{211}At	(Implanted)
6002.4 [37]	A	^{218}Po	^{218}Bi, ^{218}Pb
6050.8 [38]	A	^{212}Bi	^{212}Tl
6208.0 [39]	A	^{219}At	^{219}Bi
6288.1 [40]	A	^{220}Rn	^{220}Bi
6300.0 [38]	B	^{212}Bi	^{212}Tl
6340.0 [38]	B	^{212}Bi	^{212}Tl
6537.0 [41]	A	^{217}Po	^{217}Pb
6622.9 [36]	A	^{211}Bi	^{211}Tl
6778.3 [42]	A	^{216}Po	^{216}Pb
7386.1 [43]	A	^{215}Po	^{215}Pb
7450.3 [36]	A	^{211}Po	^{211}At
7686.82 [44]	A,B	^{214}Po	^{214}Pb, ^{214}Tl
8375.9 [45]	A,B	^{213}Po	^{213}Tl

The energy window considered in the data analysis as neutron events comprises the range from a low threshold of the 191 keV peak up to the end of the main peak of the reaction [see Eq. (1)] at 765 keV. The latter peak corresponds to the kinetic energy of the two reaction products, a triton and a proton:

$$^3\mathrm{He} + n \longrightarrow {}^3\mathrm{H} + {}^1\mathrm{H} + 765\ \mathrm{keV}. \quad (1)$$

To reduce the neutron background in BELEN two additional elements were implemented in the setup. On one hand, a PE wall with a thickness of 30 cm was installed upstream from BELEN to shield the detector from neutron background induced by the secondary beam (see Fig. 7). This wall had a central hole of 180 mm in the X direction and 70 mm in the Y direction to let the beam into SIMBA. In addition, a layer of borated rubber was attached to the rear of the PE wall in order to absorb thermalized neutrons that could eventually reach the rear side of the wall. On the other hand, the BELEN detector was surrounded by 20 cm of PE shielding (see Fig. 7) in order to moderate and absorb scattered neutrons from the surroundings.

The GSI multibranch system (MBS) [57] was used to acquire data from the FRS tracking detectors and SIMBA. This data-acquisition system (DACQ) was triggered by a scintillator at S4 with an efficiency of ∼100% for heavy ions. The MBS was also triggered by high-energy implant and low-energy β-decay events in SIMBA. On the other hand, the neutron data from BELEN were acquired by using a digital self-triggered system [58] based on SIS3302 VME digitizers from Struck Innovative Systems [59]. Each module had 8 input channels running at 100 MHz sampling rate with an ADC resolution of 16 bit. A common clock was used for time stamping the events acquired in the BELEN and MBS DACQ systems with 20 ns resolution. In this way, ion-implant versus β-decay time correlations and ion-β-neutron time correlations could be built over an arbitrarily long time window and in both forward (increasing) and backward (decreasing) time directions. The latter aspect was a key feature in the analysis stage to determine reliably the background level (see Sec. III).

III. DETERMINATION OF β-DECAY HALF-LIVES AND P_{1n} VALUES

The methodology followed here for the analysis of the β-decay half-lives is similar to the approach successfully applied in previous experiments at isotope separator on-line (ISOL) and fragmentation facilities, such as described in Refs. [16,31]. There are two fundamental aspects to this data analysis; namely, a reliable background characterization of β and neutron events and the spatial- and temporal-correlation approach. We describe first the analysis methodology from a rather general perspective and afterwards we show in detail its application to one of the largest implant statistics case, which is ^{213}Tl. The latter is also used to illustrate the background treatment in the analysis.

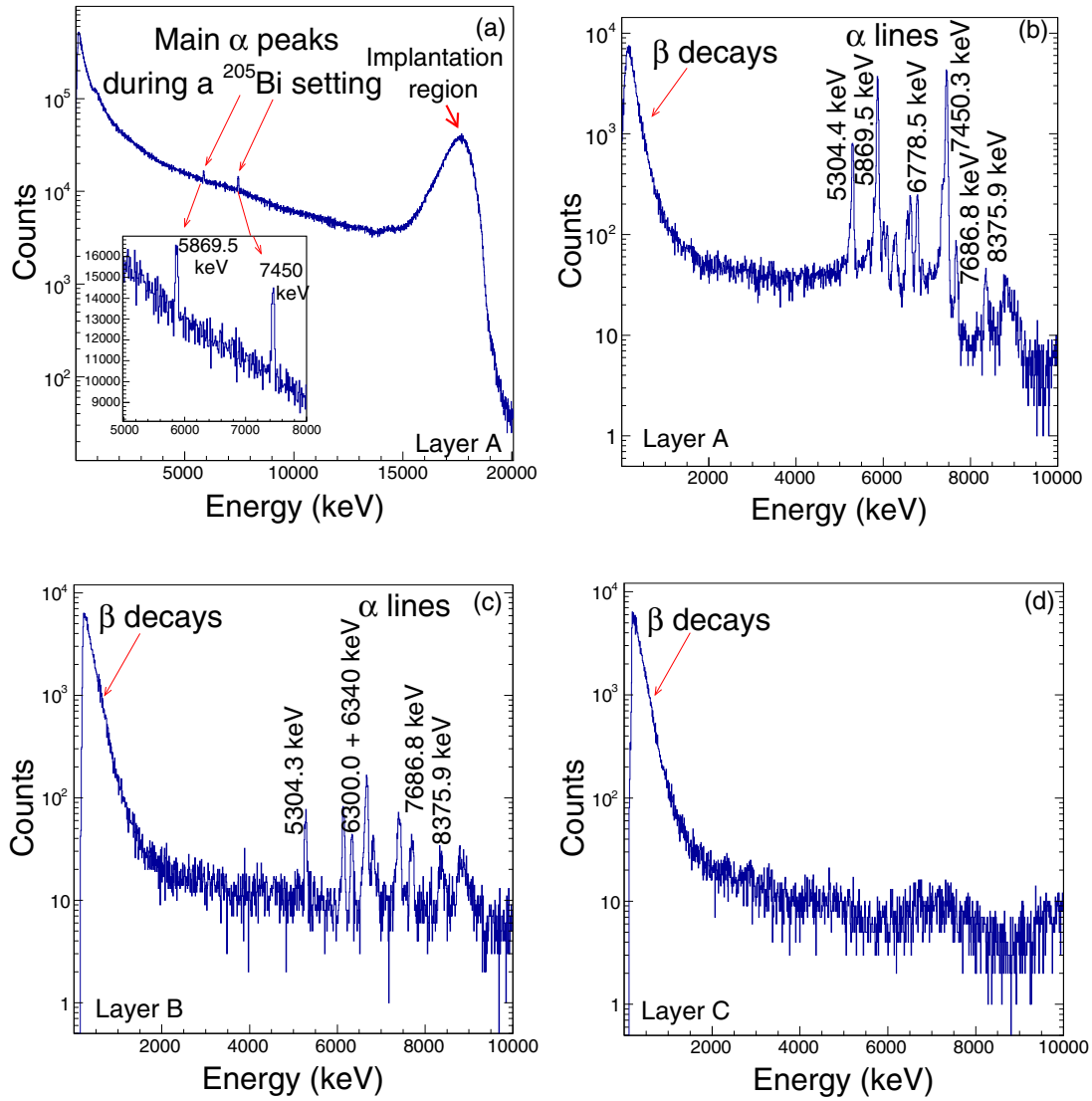

FIG. 6. Calibrated energy spectra for SIMBA layers: A (top), B and C (bottom).

Let us consider one specific isotope i. The Bateman analytical expression [60] describes the time evolution of its abundance $N_i(t)$. In this analysis we assumed that only the parent (N_1) and daughter (N_2) decays are contributing to the decay curve. This assumption is justified because all granddaughters of the analyzed nuclei are either stable nuclei or have a half-life much longer than that of the parent and daughter nuclei. The resulting expression based on this assumption is given by

$$\sum_{i=1}^{2} \lambda_i N_i(t) = [\lambda_1 N_1(t) + \lambda_2 N_2(t)], \tag{2}$$

where $\lambda_1 = \ln(2)/T_{1/2}$ is the decay constant for the implanted nucleus ($i = 1$), with unknown half-life $T_{1/2}$, and λ_2 is the decay constant of the daughter nucleus ($i = 2$). As shown below, in many cases even the contribution of the daughter nucleus was very small.

Regarding the spatial correlation, we considered an implant and a decay event to be spatially associated when the β-decay position measured in layers A, B, or C of SIMBA was within a correlation region of 3 mm^2 around the implant position measured in the same layer. Extending this condition to neighboring layers did not improve noticeably the statistics and was therefore disregarded. In general, smaller and larger

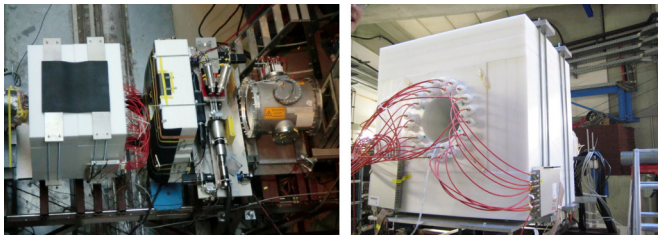

FIG. 7. (left) Top view of BELEN and the front PE shielding wall (beam enters from the right-hand side). (right) Picture of BELEN detector showing the two rings of counters, the central hole where SIMBA (see Fig. 3) was placed, and the extra 20 cm of PE shielding around.

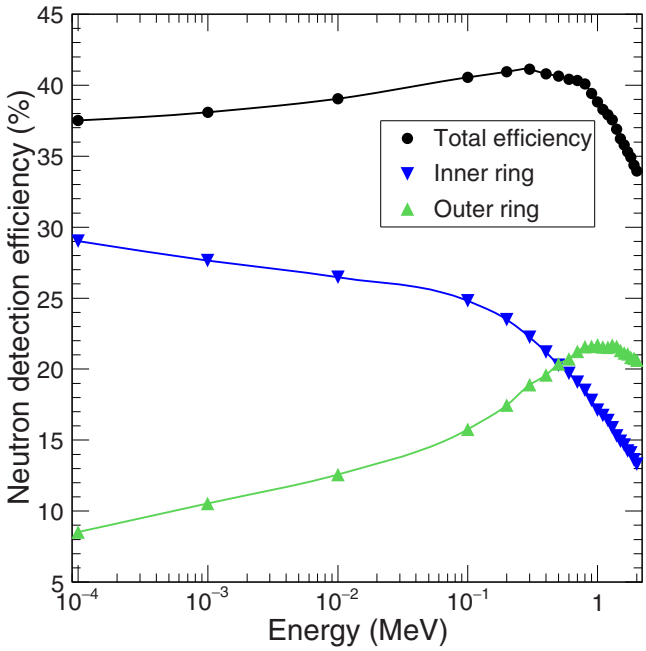

FIG. 8. MCNPX simulation of the neutron detection efficiency of BELEN as a function of the neutron energy. The lower curves refer the two rings of ^{3}He counters. See text for details.

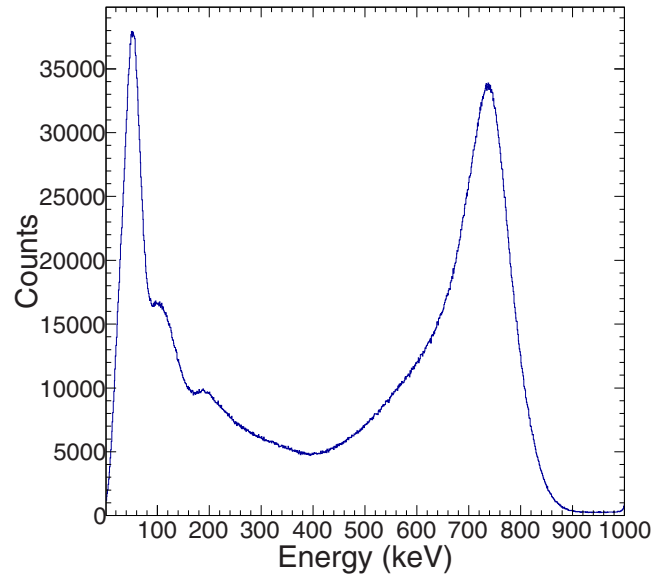

FIG. 9. Energy spectrum measured with all 30 ^{3}He tubes of BELEN during the run with the ^{211}Hg setting.

correlation areas were not found to provide a better result in terms of statistics and signal-to-background ratio in the time-correlation diagrams [27].

Regarding the time correlation, the methodology followed here consisted of building a correlation histogram for every implant of a certain species i containing its time difference with respect to all, forward and backward, β events within a broad time window $\Delta_t \gg T_{1/2}$. In this analysis we used ten times the expected half-life, $\Delta_t \simeq 10T_{1/2}$. As demonstrated below, the uncorrelated background rate is a constant value, which can be referred to as b. In this case, the probability density function describing the time dependence of the correlation distribution is given by [61]

$$\rho(\lambda_1,t) = \varepsilon_\beta b + \varepsilon_\beta \lambda_1 e^{-\lambda_1 t} + \varepsilon_\beta \frac{\lambda_1\lambda_2}{\lambda_1-\lambda_2}(e^{-\lambda_2 t} - e^{-\lambda_1 t}), \quad (3)$$

where ε_β is the β-detection efficiency in SIMBA. Thus, for a certain number $N_1(0)$ of implanted events, the total number N_β of β particles detected at a time t with respect to the implantation time ($t = 0$) is given by

$$N_\beta^{All\beta}(t) = N_1(0)\rho(\lambda_1,t)\Delta t = \varepsilon_\beta[\lambda_1 N_1(t) + \lambda_2 N_2(t) + b]\Delta t, \quad (4)$$

where $N_\beta^{All\beta}(t)$ is the total number of detected decays at a time t, b is the β background normalized and corrected by ε_β, and Δt corresponds to the bin time width used in the implant-β time-correlation histogram. The time evolution of the parent abundance is described by $N_1(t) = N_1(0)e^{-\lambda_1 t}$, whereas the contribution of the daughter is given by $N_2(t) = N_1(0)\frac{\lambda_1}{\lambda_1-\lambda_2}(e^{-\lambda_2 t} - e^{-\lambda_1 t})$, assuming $N_2(0) = 0$. In the data analysis, the common factor $N_1(0)\varepsilon_\beta$ in Eq. (4) is derived from the first bin in the correlation diagram [27]. In this way the quantity of interest ($T_{1/2}$) can be reliably determined without knowing explicitly the β-detection efficiency.

A. Reference analysis of ^{213}Tl half-life

The thallium isotope ^{213}Tl was implanted with large statistics (1015 implants), so we used this case to establish the analysis methodology on a reliable statistical basis. The β background showed a dependency with the time structure of the pulsed primary beam. Indeed, during beam extraction from SIS (1 s) the overall background level of β-like events in SIMBA was ~40% higher than during the time-interval between spills [27]. This feature led to a better signal-to-background ratio in the implant-β time-correlation histograms when only β-events outside of the spill time intervals were considered in the correlations, when compared with the same diagram including β-events inside and outside the spill. With this restriction in mind, the background level evaluation was based on time backward ($t < 0$) implant-β correlations, i.e., the time difference between each implant and all the β events occurring before it, within a broad time window ($\Delta t \simeq 10T_{1/2}$) and in the same correlation area used in the forward analysis of 3×3 mm^2. The background level thus determined allows one to adjust the parameter b in Eq. (3). This approach is illustrated in Fig. 10 for the case of ^{213}Tl, which shows backward (negative) and forward (positive) implant-β correlations. The contribution to the measured β activity from decays of other nuclei can be assumed to be negligible due to the very low average implantation rate of 2×10^{-5} ions s^{-1} pixel^{-1}. By using Eq. (4), a binned maximum likelihood (ML) [62] analysis of the time correlation histogram was carried out, which yielded a half-life for ^{213}Tl of $T_{1/2} = 23.8 \pm 4.4$ s. Comparison with other literature values is made in Sec. IV.

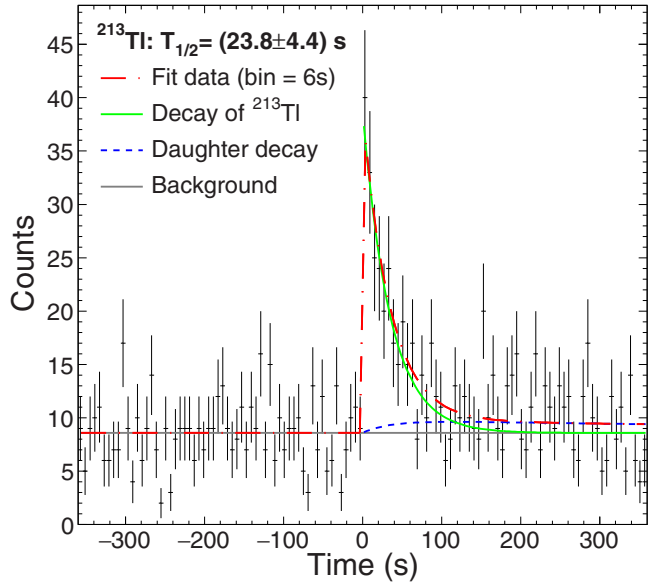

FIG. 10. ^{213}Tl implant-β time diagram using a correlation area of 3×3 mm^2 and β events detected outside of the spill. The red line shows the result of a binned maximum likelihood (ML) analysis. The decay curve shows mostly the contribution of ^{213}Tl decay (green line), with a minor contribution from the daughter ^{213}Pb (dashed blue line).

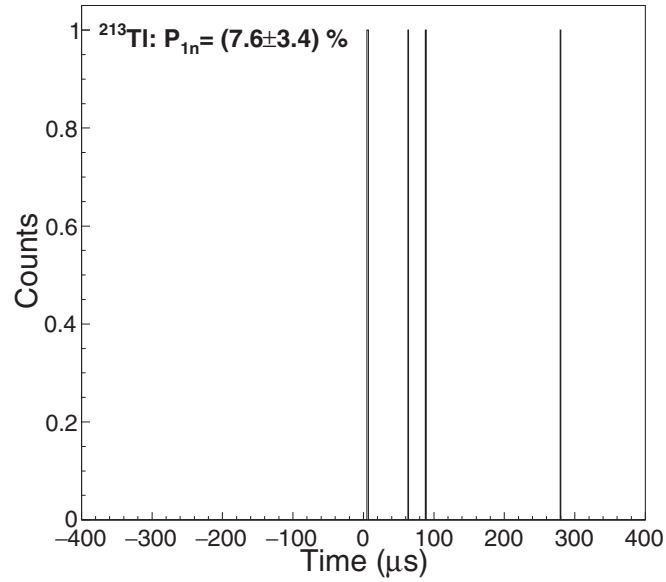

FIG. 11. β-neutron correlation events during the ^{213}Tl implant-β correlation time.

B. Neutron branching ratio for ^{213}Tl

The implant-β neutron correlations were analyzed by selecting a correlation window of $\Delta_t^n = 400$ μs forward and backward in time, following each β detection. This time interval was determined according to the expected neutron moderation time in polyethylene. Considering the β efficiency ε_β as a constant value over the range of energies of interest, the P_{1n} value can be directly obtained from the subtraction of time-forward and time-backward β-neutron correlated events,

$$P_{1n}(\%) = \frac{1}{\varepsilon_n} \frac{N_{\beta n}^{\mathrm{fwd}} - N_{\beta n}^{\mathrm{bkd}}}{N_\beta} \times 100, \qquad (5)$$

where ε_n is the BELEN neutron efficiency, $N_{\beta n}^{\mathrm{fwd}}$ is the number of forward correlated implant-β-neutron events, and N_β is the number of parent β decays. $N_{\beta n}^{\mathrm{bkd}}$ designates the backward β-neutron correlations, which were used to define the uncorrelated neutron background level. The efficiency can be considered flat over the energy range of interest according to the $Q_{\beta n}$ values of the implanted isotopes (100 keV to 2.5 MeV; [55,56]), with a constant value of 38% and a relative uncertainty of 5% (see Fig. 8). This overall uncertainty includes the contributions of statistical errors for $N_{\beta n}^{\mathrm{fwd}}$, $N_{\beta n}^{\mathrm{bkd}}$, and N_β together with the uncertainty for the BELEN detector efficiency from the fluctuations over the energy range. For ^{213}Tl we measured five forward and no backward correlated neutrons (Fig. 11), which yielded a P_{1n} value of 7.6% ± 3.4%.

C. Thallium isotopes: $^{211-216}$Tl

Five more thallium isotopes were measured and their β-decay half-lives and neutron-branching ratios were analyzed following the approach described above for ^{213}Tl. The implant-β time-correlation histograms for all of them, $^{211,212,214-216}$Tl are shown in Fig. 12. The binned ML analysis (dashed-dotted line on diagrams) yields $T_{1/2} = 76.5 \pm 17.8$ s for ^{211}Tl, $T_{1/2} = 30.9 \pm 8.0$ s for ^{212}Tl, and $T_{1/2} = 11.0 \pm 2.4$ s for ^{214}Tl. An almost negligible contribution from the much slower decay of the daughter nuclei (^{211,212,214}Pb) can be observed in these three cases. The most exotic thallium species implanted, ^{215,216}Tl, were measured with rather limited statistics of only 281 and 99 implants, respectively. In this case, we noticed a slight improvement in the signal-to-background ratio in the correlation histograms when the correlation area was enlarged from 3×3 mm^2 to 5×5 mm^2. The ML analysis also shown in diagrams of Fig. 12 yielded a half-lives $T_{1/2} = 9.7 \pm 3.8$ s for ^{215}Tl and $T_{1/2} = 5.9 \pm 3.3$ s for ^{216}Tl.

The neutron-data analysis showed the presence of only one correlated implant-β-neutron event for each of ^{211,212,215}Tl, which yields neutron-branching ratios of 2.2(2.2)%, 1.8(1.8)% and 4.6(4.6)%, respectively. For these three cases, given the low number of events compatible with the physical boundary, we have alternatively calculated a conservative upper limit based on the Bayesian approach [63], which yields upper limits of 10%, 8%, and 20% at a confidence level (CL) of 95%. On the other hand, with BELEN we were able to observe a rather large number (10) of implant-β-neutron correlated events for ^{214}Tl (histogram also shown in Fig. 12), resulting in a P_{1n} value of 34.3% ± 12.2%. No single correlated or uncorrelated event was detected for ^{216}Tl which, according to the implantation statistics obtained, led to an upper limit of 11.5% and a Bayesian upper limit of $P_{1n} < 52\%$ at the 95% CL. Concerning the other implanted species, ^{209,210}Tl, the implantation statistics was not enough to determine either their half-lives or the neutron-branching ratios.

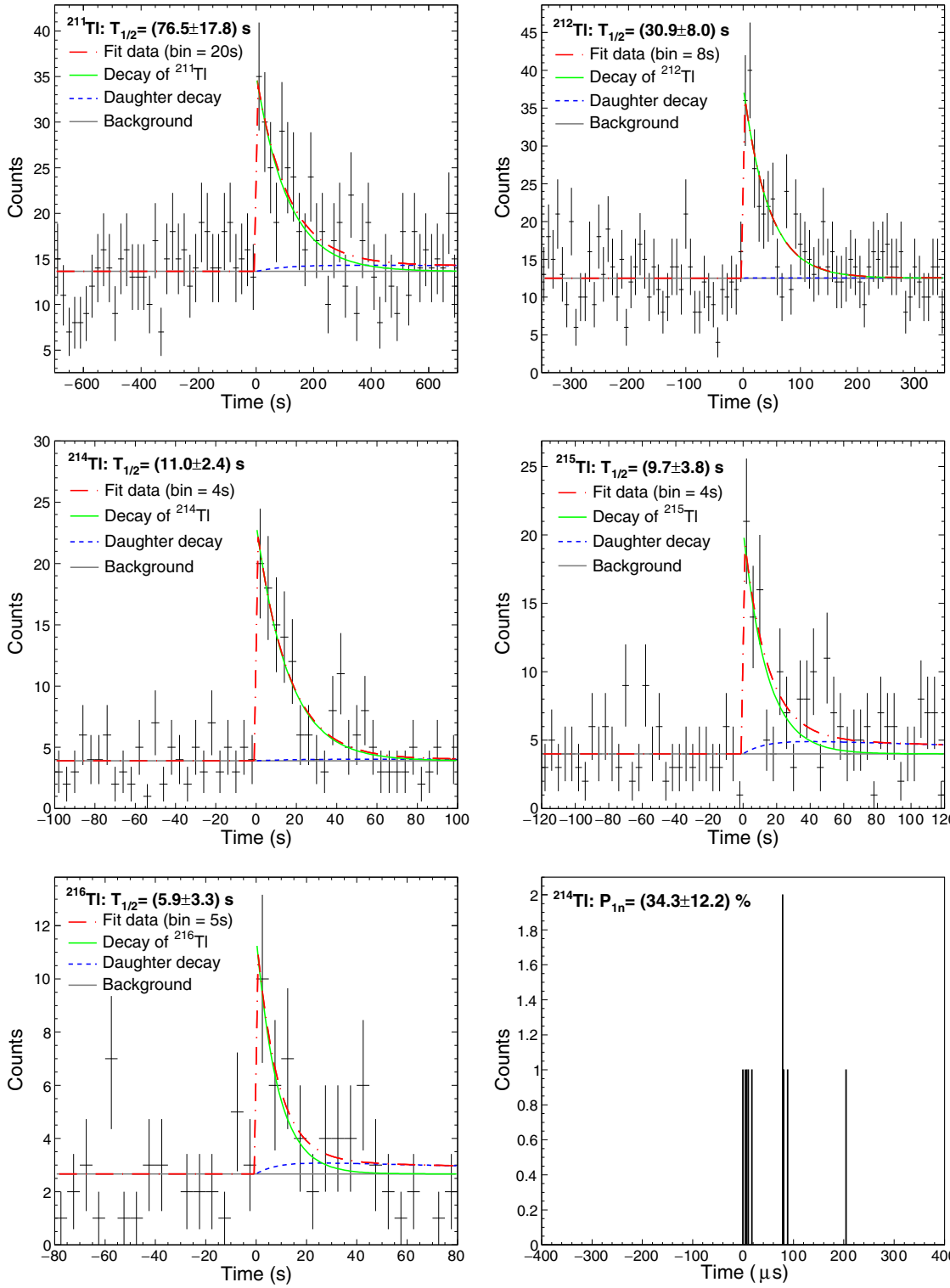

FIG. 12. Implant-β correlation histograms for $^{211,212,214-216}$Tl. The diagrams for ^{215,216}Tl were obtained by using a correlation area of 5×5 mm^2. The last histogram corresponds to the implant-β-neutron time correlations for ^{214}Tl.

D. Lead isotopes: $^{215-218}$Pb

The lead isotopes $^{212-219}$Pb were identified in the FRS and implanted in SIMBA. The $^{215-218}$Pb nuclei were implanted with enough statistics for a reliable half-life analysis. ^{214}Pb was also implanted with large statistics (see Fig. 5), but its half-life of 1608 ± 54 s [64] was too long for our analysis methodology and instrumentation. The ML analyses for the implant-β correlation diagrams of $^{215-218}$Pb are shown in Fig. 13. The ^{215}Pb analysis yielded a half-life of $T_{1/2} = 98.4 \pm 30.8$ s. As

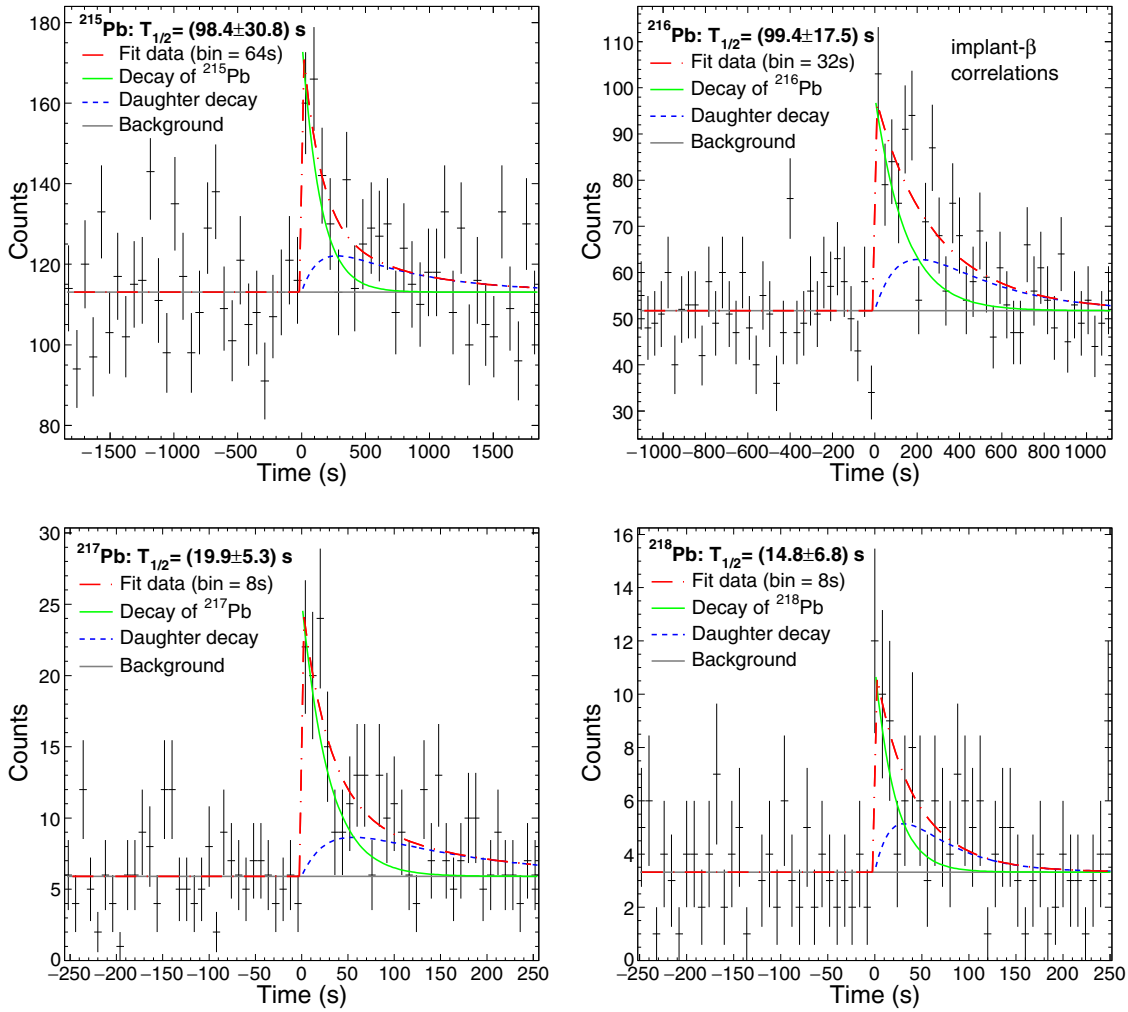

FIG. 13. Half-life analysis for implant-β correlation diagrams of $^{215-218}$Pb.

can be observed on its diagram, contributions from ^{215}Pb and its daughter ^{215}Bi are present in the correlation histogram. For the case of the measurement of ^{216}Pb, it allowed us to carry out a cross-check of the aforementioned analysis methodology, because its half-life can be determined by means of two different methods: implant-β and implant-α correlations. The former is also illustrated in Fig. 13, which shows the implant-β correlation and the result of the ML analysis. On the other hand, the peak of α particles at 6778.3 keV, clearly identified in the energy spectrum of SIMBA [see Fig. 6(b)], corresponds to the decay of its granddaughter nucleus ^{216}Po. Taking into account that the half-life of ^{216}Po, 145 ± 2 ms [40], is much shorter than that of the direct daughter ^{216}Bi, 2.25 ± 5 min [40], it was possible to apply the method described in Ref. [65] to obtain the half-life of ^{216}Pb. With this method we determined a half-life of $T_{1/2} = 99.4 \pm 11.7$ s (see diagram of Fig. 14) which is in perfect agreement with the one obtained applying the conventional method described above for implant-β time correlation, $T_{1/2} = 99.4 \pm 17.5$ s. The accuracy in the analysis of ^{217}Pb and ^{218}Pb was mainly limited by the implantation statistics, where there was 436 and 235 implants, respectively. However, a reliable ML analysis was possible from their implant-β correlation diagrams, as shown in the low diagrams of Fig. 13. The resulting half-lives were $T_{1/2} = 19.9 \pm 5.3$ s for ^{217}Pb and $T_{1/2} = 14.8 \pm 6.8$ s for ^{218}Pb. According to the negative $Q_{\beta n}$ values for all these lead isotopes, no neutron branching emission is expected for them.

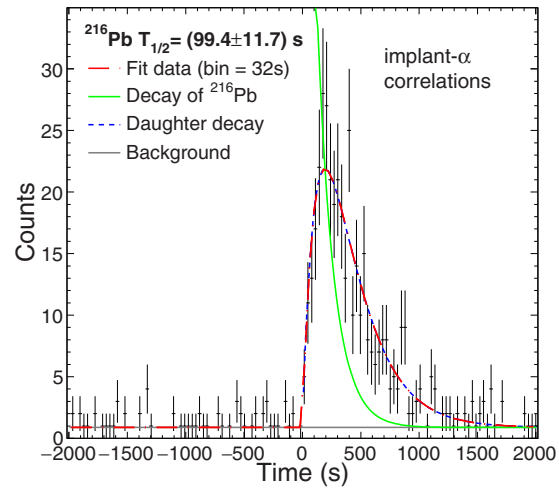

FIG. 14. Half-life analysis of ^{216}Pb via implant-α correlations.

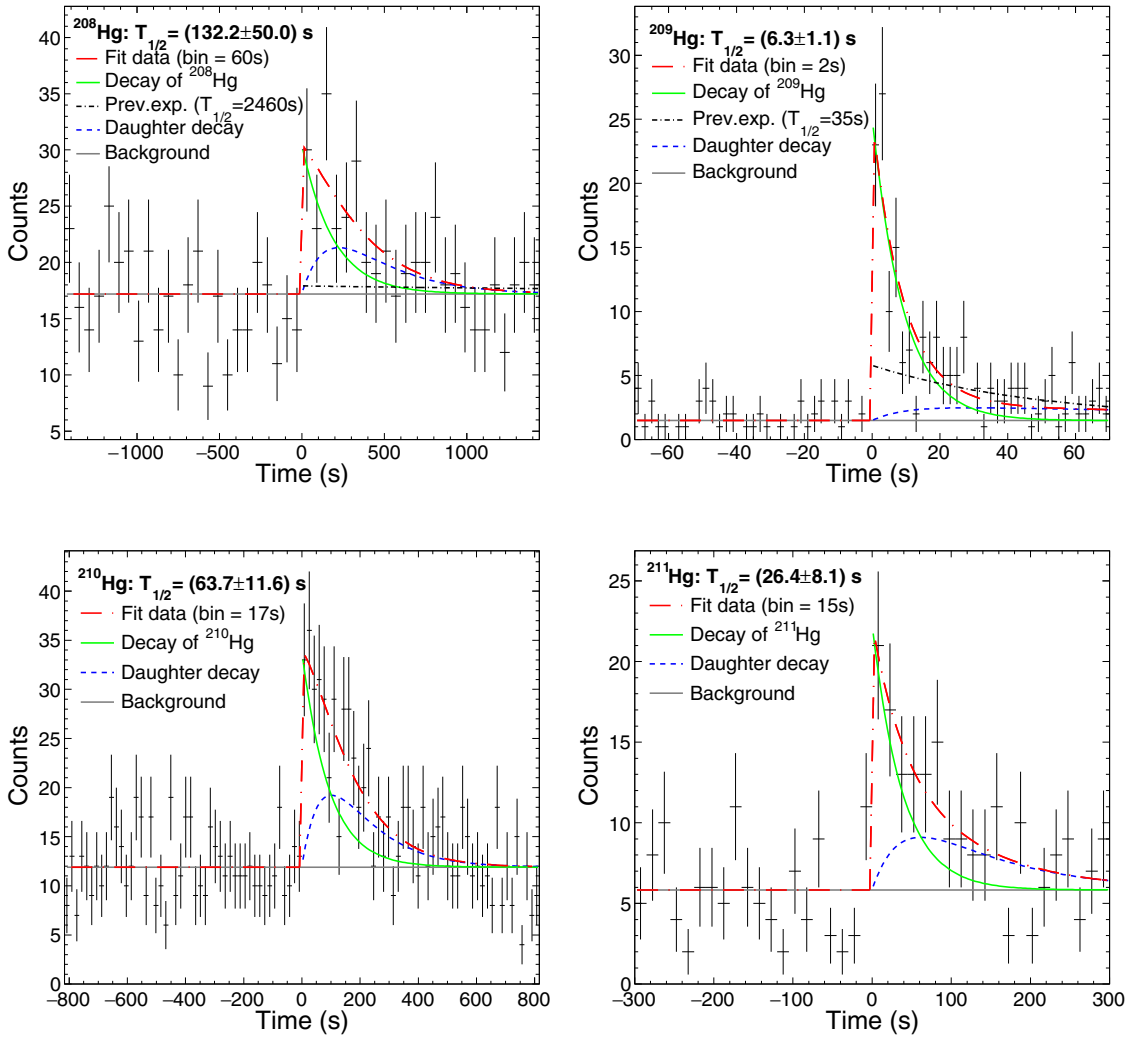

FIG. 15. Implant-β correlation diagrams for $^{208-211}$Hg. In the ^{208}Hg and ^{209}Hg diagrams are shown the parent and daughter contributions to the measured decay curve, and the decay of previous half-lives (see text for details).

E. Mercury isotopes: $^{208-211}$Hg

From the eight mercury isotopes identified, $^{206-213}$Hg, implant statistics were high enough to analyze four of them reliably, $^{208-211}$Hg. The decay curve is strongly determined by the number of ion implants, as well as by the value of the half-life. Thus, for ^{208}Hg, with low implantation statistics (220 events) and a relatively long half-life obtained from the ML analysis, $T_{1/2} = 132.2 \pm 50$ s, the statistical uncertainty was 38%. On the other hand, ^{209}Hg has a factor of about two more implants (583 events) and a shorter half-life ($T_{1/2} = 6.3 \pm 1.1$ s), which leads to an uncertainty much lower, 17%. An intermediate situation is found for the remaining two mercury isotopes, ^{210,211}Hg, for which the half-life analysis yielded $T_{1/2} = 63.7 \pm 11.6$ s and $T_{1/2} = 26.4 \pm 8.1$ s, respectively. In the latter case, the value obtained in the present work for the half-life of ^{211}Tl was employed in the analysis. All of the implant-β correlation diagrams for these cases are shown in diagrams of Fig. 15. Regarding the neutron emission branching ratio, for ^{210}Hg and ^{211}Hg one implant-β-neutron event has been detected in the forward (moderation) time window for

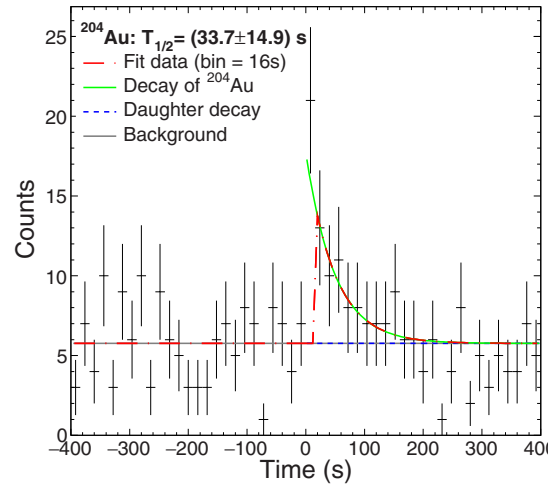

FIG. 16. ^{204}Au implant-β diagram. The correlation area used was 25 mm^2 and implant-β events inside the spill were included in the analysis.

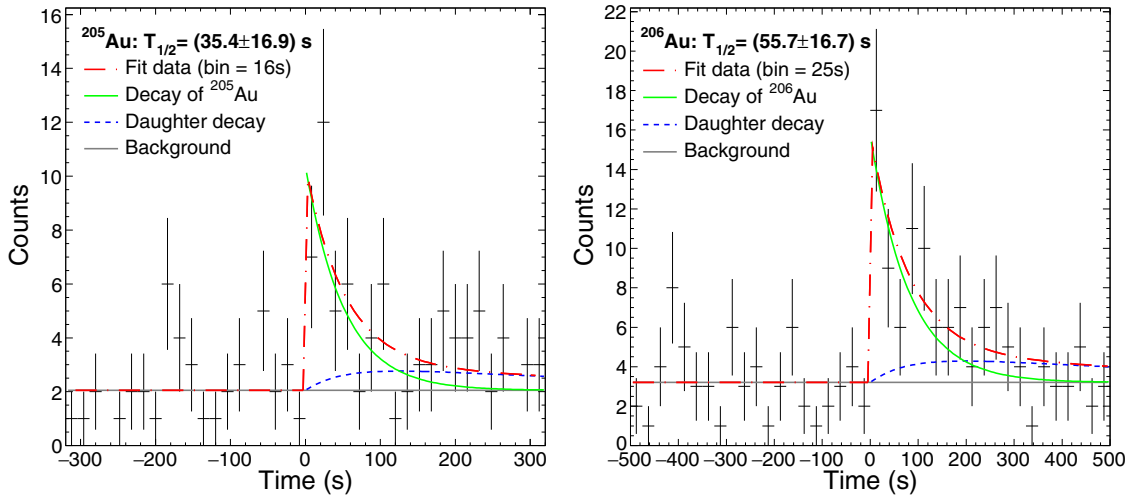

FIG. 17. Analysis of the implant-β correlation diagrams for ^{205}Au and ^{206}Au.

each nucleus. This measurement yields neutron-branching ratios of 2.2(2.2)% and 6.3(6.3)%, respectively. For these cases the calculated conservative upper limit based on the Bayesian approach [63] yields upper constraints of 10%, and 28% at a CL of 95%.

F. Gold isotopes: $^{204-206}$Au

The $^{203-209}$Au isotopes were identified in this measurement, but the implantation statistics was only high enough to analyze three of them, $^{204-206}$Au. In the case of ^{204}Au (see Fig. 16) we also found a slight improvement of the decay curve when the correlation area was enlarged from 1 pixel (9 mm^2) to 2 pixels (25 mm^2) around the implant location and included in the correlation those implant-β events detected during the spill time. These provide a better sensitivity for the analysis, which yields a half-life of $T_{1/2} = 33.7 \pm 14.9$ s. For the cases of ^{205}Au and ^{206}Au, both with ~100 implants, the ML analysis of the implant-β correlation diagrams yielded half-lives of $T_{1/2} = 35.4 \pm 16.9$ s and $T_{1/2} = 55.7 \pm 16.7$ s, respectively. Figure 17 shows the analysis for these two gold isotopes.

G. Bismuth isotopes: $^{218-220}$Bi

Bismuth was the heaviest element implanted in SIMBA and we were able to determine the half-lives of three isotopes, $^{218-220}$Bi. The ML analysis of ^{218}Bi yields a half-life of $T_{1/2} = 38.5 \pm 21.6$ s and, as can be seen in the diagram in Fig. 18, the β contribution comes only from its own decay, as its daughter (^{218}Pb) is an α emitter. The half-life analysis for ^{219}Bi yields $T_{1/2} = 8.7 \pm 2.9$ s (see the diagram also on Fig. 18) and it includes the recent published half-life for its daughter, ^{219}Po, $T_{1/2} = 620 \pm 59$ s [66].

For the β-decay analysis of ^{220}Bi one has to take into account that the half-life of its daughter nucleus ^{220}Po is still unknown. Thus, our analysis provides a range of possible half-life values for ^{220}Bi, which spans between 4 and 15 s. The bold marker in Fig. 19 represents the ^{220}Bi half-life using the

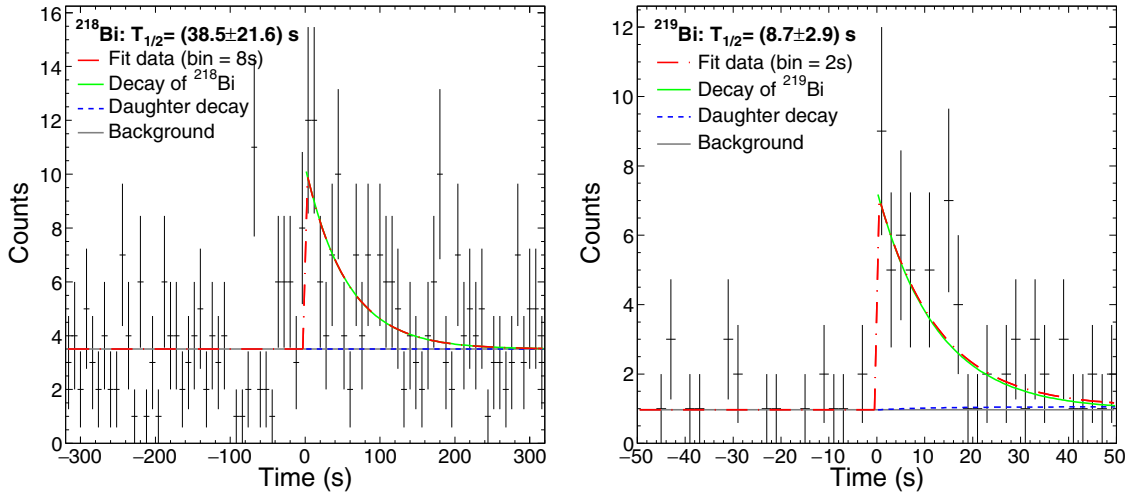

FIG. 18. Analysis of the implant-β correlation diagrams for ^{218}Bi and ^{219}Bi.

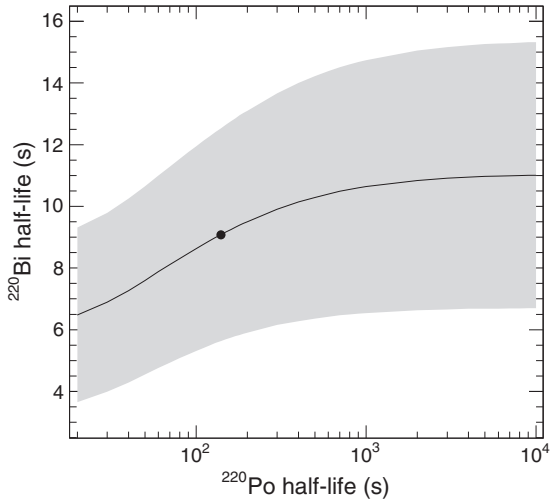

FIG. 19. ^{220}Bi half-life measured by varying the time of unknown daughter half-life in a wide range. The dot indicates the half-life given by using the finite-range droplet model plus the quasi-particle random-phase approximation (FRDM + QRPA) theoretical value for ^{220}Po, $T_{1/2} = 138.47$ s.

theoretical prediction calculated by FRDM+QRPA model [67] for the half-life of ^{220}Po, $T_{1/2} = 138.47$ s.

IV. SUMMARY AND DISCUSSION

This section provides a summary of the main results obtained in this work, as well as a comparison with all previous experimental results and the theoretical predictions of FRDM + QRPA [67] and DF3 + cQRPA [68] models. A detailed comparison with the more recent calculations of Refs. [69,70] can be found in Ref. [19]. In summary, half-life values for 20 neutron-rich isotopes of Au, Hg, Tl, Pb, and Bi have been determined experimentally, as well as neutron-branching ratios (or upper limits) for eight of them. The results are displayed in Figs. 20 and 21, and listed in Tables II and III. As some of the analyzed isotopes are not expected to be neutron emitters according to their $Q_{\beta n}$ values (see the last column of Table II), due to the low statistics available, the neutron-emission analysis has been focused on those with large-enough $Q_{\beta n}$. For comparison purposes, previously published theoretical and experimental half-life values have also been included in Fig. 20.

Apart from the discrepancies found for the ^{208,209}Hg isotopes, a rather good agreement is found between the present results and previously published experimental data. In the case of gold isotopes, all half-lives are fully compatible with those reported in previous measurements [18,73–76], which are in reasonable agreement with DF3 + cQRPA for $N \leqslant 126$. For ^{206}Au ($N = 126$) the half-life obtained confirms the recent value published in Ref. [76] and both differ from the DF3 + cQRPA value and the trends predicted by the available theoretical models. Whether this "gold anomaly" is related to effects changing the occupation of the $\nu i_{11/2}$ orbital, or due to a weakening of the spin-orbit field caused by the tensor force [80], or might be due to the recently proposed three-body force mechanism [81,82] remains an open question

TABLE II. P_n results compared with theoretical predictions for the measured isotopes.

Nuclei	N	P_n(%) (this work)	FRDM + QRPA (%) [67]	DF3 + cQRPA (%) [71]	RHB + RQRPA (%) [70]	KTUY (%) [69]	QRPA-HF (%) [72]	$Q_{\beta n}$(keV) [55,56] (extr. = extrapolated)
^{204}Au	125		0.0	0.0	0.1	0.0		−3453 ± 200 (extr.)
^{205}Au	126		0.0	0.0	0.2	0.0		−2151 ± 196 (extr.)
^{206}Au	127		0.0	0.0	0.5	0.0	0.0	2 ±298 (extr.)
^{208}Hg	128		0.0	3.2	0.3	0.0		−303.32 ± 31.23
^{209}Hg	129		0.0	2.8	0.5	0.0		34 ±149 (extr.)
^{210}Hg	130	2.2 ±2.2	0.0	9.3	0.6	0.0	71	201 ±196 (extr.)
^{211}Hg	131	6.3 ±6.3	0.81	7.5	0.8	0.0	11	551 ±196 (extr.)
^{211}Tl	130	2.2 ±2.2	0.04	0.95	1.2	0.28		578.67 ±41.95
^{212}Tl	131	1.8 ±1.8	0.56		1.3	0.23	0.0	869 ±200 (extr.)
^{213}Tl	132	7.6 ±3.4	13.26	2.93	6.8	1.93	100	1259.73 ±27.10
^{214}Tl	133	34.3 ±12.2	10.38		10	1.56	66	1595 ±196 (extr.)
^{215}Tl	134	4.6 ±4.6	55.24		14.2	5.54	100	2021 ±298 (extr.)
^{216}Tl	135	<11.5	55.36		17	4.45	96	2230 ±315 (extr.)
^{215}Pb	133		0.0	0.0	0.3	0.0		−2455 ± 102 (extr.)
^{216}Pb	134		0.0	0.0	0.3	0.0	0.0	−2240 ± 196 (extr.)
^{217}Pb	135		0.0	0.0	0.4	0.0	0.0	−1705 ± 298 (extr.)
^{218}Pb	136		0.0	0.0	0.4	0.0	0.0	−1348 ± 299 (extr.)
^{218}Bi	135		0.0		1.2	0.0	0.0	−740.61 ± 27.73
^{219}Bi	136		0.06		0.3	0.0	0.0	−148 ± 196 (extr.).
^{220}Bi	137		0.01		0.4	0.0	0.0	66.0 ±298 (extr.)

TABLE III. Half-lives ($T_{1/2}$) results, and some of the previous experimental data and theoretical predictions.

Nuclei	N	Implanted ions	$T_{1/2}^{expt}$ (s) (this work)	Previous $T_{1/2}^{expt}$ (s)	FRDM + QRPA (s) [67]	DF3 + cQRPA (s) [68]
^{204}Au	125	54	33.7 ±14.9	39.8 ±0.9 [73]	455.3	42.4
				37.2 ±0.8 [18]		
				40 ±3 [74]		
^{205}Au	126	103	35.4 ±16.9	31 ±2 [75]	222.0	18.7
				32.5 ±1.4 [18]		
^{206}Au	127	106	55.7 ±16.7	40.0 ±15.0 [76]	21.3	0.72
^{208}Hg	128	220	132.2 ±50.0	2460^{+300}_{-240} [77]	168.9	12.1
^{209}Hg	129	583	6.3 ±1.1	35.0^{+9}_{-6} [77]	33.6	3.7
^{210}Hg	130	512	63.7 ±11.6	>300 ns	41.2	5.2
^{211}Hg	131	253	26.4 ±8.1	>300 ns	14.9	1.9
^{211}Tl	130	483	76.5 ±17.8	88^{+46}_{-29} [78]	70.9	114.9
^{212}Tl	131	1056	30.9 ±8.0	96^{+42}_{-38} [78]	29.0	
^{213}Tl	132	1015	23.8 ±4.4	101^{+486}_{-46} [30]	32.4	70.4
				46^{+55}_{-26} [78]		
^{214}Tl	133	598	11.0 ±2.4	>300 ns	14.4	
^{215}Tl	134	281	9.7 ±3.8	>300 ns	7.8	
^{216}Tl	135	99	5.9 ±3.3	>300 ns	2.8	
^{215}Pb	133	1079	98.4 ±30.8	147 ±12 [79]	282.5	27.1
				160 ±40 [65]		
^{216}Pb	134	1005	99.4 ±11.7	>300 ns	852.2	52.0
^{217}Pb	135	436	19.9 ±5.3	>300 ns	104.9	8.5
^{218}Pb	136	235	14.8 ±6.8	>300 ns	66.3	28.4
^{218}Bi	135	294	38.5 ±21.6	33 ±1 [64]	2.92	
				36 ±14 [78]		
^{219}Bi	136	306	8.7 ±2.9	22 ±7 [78]	26.54	
^{220}Bi	137	176	9.5 ±5.7	>300 ns	5.17	

which calls for more detailed theoretical studies and further specific experiments allowing for reconstruction of the decay scheme.

Concerning Hg isotopes, as discussed in Ref. [19], recent measurements at the CERN On-Line Isotope Mass Separator (ISOLDE) facility [83] indicate that the half-lives of the ^{208,209}Hg nuclei are much shorter than the values reported in Ref. [77] and, therefore, this discrepancy will not be discussed further. Theoretical half-life predictions by FRDM + QRPA show a fairly good agreement with the measured values, with the only exception being ^{209}Hg. Interestingly, the opposite behavior is found regarding DF3 + cQRPA predictions. This feature might reflect that first-forbidden transitions still play a dominant role in the β decay of ^{209}Hg. Further high-resolution spectroscopy measurements are needed in order to shed light on this aspect.

Regarding the thallium isotopes, previous half-lives were obtained in another experiment by using a similar experimental setup, but with a completely different analysis approach [78,84]. In summary, a good agreement is found for ^{211}Tl, whereas the half-lives of ^{212}Tl and ^{213}Tl differ by factors of two to three. It is worth emphasizing the overall good agreement for the thallium chain between the present results and FRDM + QRPA predictions, including the case of the most exotic nuclei reported here for the first time, $^{214–216}$Tl. This result seems to indicate the rather low relevance of first forbidden (FF) transitions in the $N \geqslant 126$ mass region, as discussed in Ref. [19].

The analysis of the lead isotopes includes three new half-lives, $^{216–218}$Pb. The half-life obtained for ^{215}Pb is in reasonable agreement with the two previous measurements [65,79]. Along the lead isotopic chain, the FRDM + QRPA model overestimates the experimental values by factors between three to nine. The values predicted by DF3 + cQRPA are, on average, slightly closer to the measured half-lives, but the mass (neutron number) dependency of the half-life is not satisfactorily reproduced by either of these two models.

For the bismuth chain the FRDM + QRPA predictions agree reasonably well with the heaviest measured nuclei $^{219–220}$Bi, whereas almost one order-of-magnitude difference

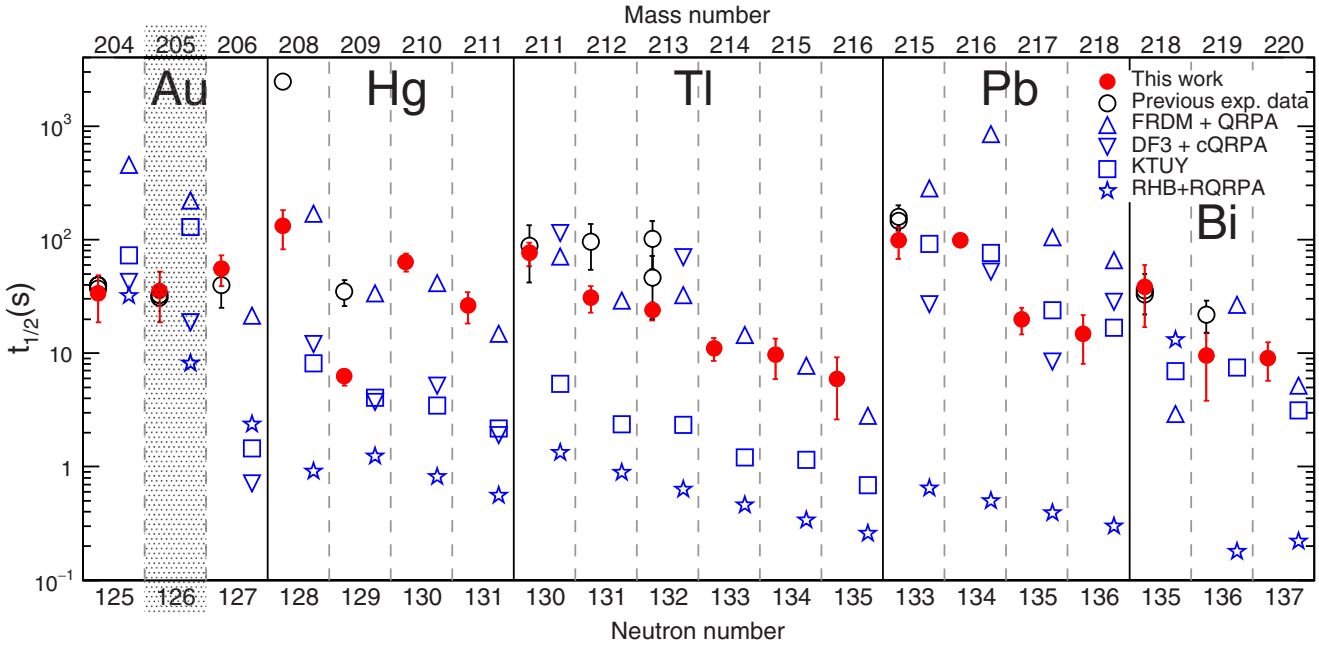

FIG. 20. Half-lives obtained in this work (red dots). Previous experimental values (open black circles). The blue symbols correspond to the theoretical values from different models: triangles for FRDM + QRPA [67] and DF3 + cQRPA [68], squares for the calculations from KTUY [69], and stars for the RHB + RQRPA [70] model. See text and Table III for details.

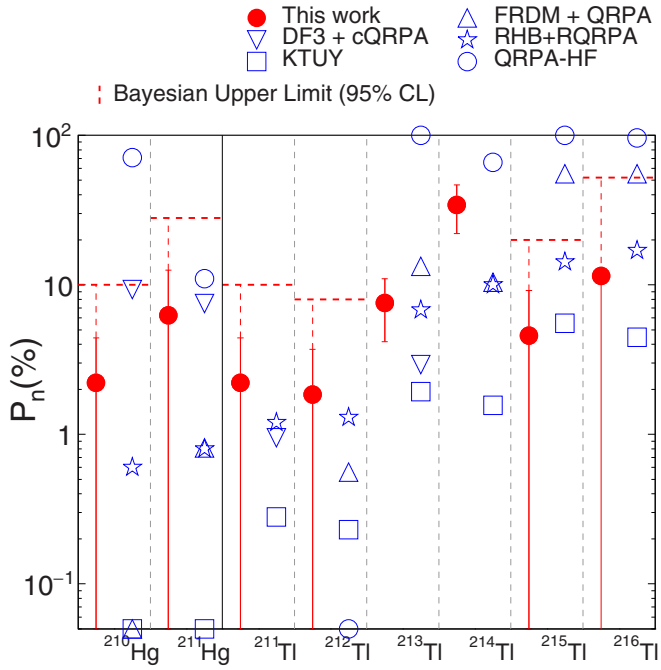

FIG. 21. Experimental neutron-branching ratios and upper limits obtained in this work (red dots) and conservative upper-limit based on the Bayesian approach at a CL of 95% (red dashed lines). The blue triangles correspond to the theoretical predictions of the FRDM + QRPA [67] and DF3 + cQRPA [68] models. Blue squares and stars show KTUY [69] and RHB + RQRPA [70], respectively, and blue circles show recent new calculations, QRPA-HF, by Ref. [72]. See text and Table II for details.

is found for ^{218}Bi. The latter half-life is, however, rather well established experimentally [78]. The result quoted in this work for the half-life of ^{220}Bi, 4–15 s (see Fig. 19), can be redetermined more accurately once the half-life of ^{220}Po is measured.

The neutron-branching ratios determined in this work represent the first set of experimental data available in this mass region. Therefore, the values reported here can only be compared with theoretical predictions. Both theoretical and experimental P_{1n} values are listed in Table II and displayed in Fig. 21.

In summary, the agreement between theory and experiment is rather good for the Hg and Tl isotopes with masses between 208 and 214. However, for the two heaviest thallium nuclei ^{215,216}Tl, KTUY [69] and RHB + RQRPA [70] models are in agreement but the other theoretical predictions of the neutron emission overestimate substantially the experimental results obtained.

V. CONCLUSIONS

Since both the half-life and the neutron emission probability are integral quantities of the β decay, it is difficult to explain why the FRDM + QRPA reproduces so well the average decay strength over the full Q_β window (see Fig. 20) along the chain of measured Tl isotopes, whereas it seems to fail dramatically in the upper energy range of ^{215,216}Tl, beyond the neutron separation energy of the daughter nuclei, as deduced from their neutron-branching ratios. At first sight, one is tempted to attribute such a discrepancy to the possible contribution of high-energy first forbidden (FF) transitions populating low-lying levels in the daughter nuclei and thus hindering the emission of neutrons. Nevertheless, this interpretation is at

variance with the overall systematics found in the $N \geqslant 126$ region [18,19,65,76,78], where Gamow–Teller (GT) transitions seem to play a dominant role in general. At present, the only plausible explanation for such a feature could be that the overall strength of the β decay is overestimated in FRDM + QRPA, both in the full Q_β and in the upper energy window $Q_{\beta n}$. As reported in Ref. [19], more advanced microscopic models such as RHB + RQRPA [70] and KTUY [69] show an inverted behavior, yielding good predictions for the P_{1n} values, but discrepant values for the half-lives, thus not improving the situation. Recent calculations based on an improved QRPA and HF theory [72], included in Fig. 21, also show large discrepancies. Clearly, more β-decay measurements and theoretical efforts are needed in this mass region to gain a better understanding of the underlying nuclear structure effects, as well as to guide global theoretical models far-off stability.

ACKNOWLEDGMENTS

This work was supported by the Spanish Ministerio de Economia y Competitividad under Grants No. FPA2011-28770-C03-03, No. FPA2008-04972-C03-03, No. AIC-D-2011-0705, No. FPA2011-24553, No. FPA2008-6419, No. FPA2010-17142, No. FPA2014-52823-C2-1-P, No. FPA2014-52823-C2-2-P, and No. CPAN CSD-2007-00042 (Ingenio2010), and the program Severo Ochoa (SEV-2014-0398). I.D. and M.M. were supported by the German Helmholtz Association via the Young Investigators Grant VH-NG 627 (LISA- Lifetime Spectroscopy for Astrophysics) and the Nuclear Astrophysics Virtual Institute (VH-VI-417), and by the German Bundesministerium für Bildung und Forschung under No. 06MT7178 / 05P12WOFNF. R.C.F. acknowledges the support of the Spanish Nuclear Security Council (CSN) under a grant of Catedra Argos. UK authors acknowledge the support of the UK Science & Technology Facilities Council (STFC) under Grant No. ST/F012012/1. Yu.A.L. acknowledges support from Helmholtz-CAS Joint Research Group (HCJRG-108). R.C.F. and I.D. are also supported by the National Research Council of Canada (NSERC) Discovery Grants SAPIN-2014-00028 and RGPAS 462257-2014 at TRIUMF.

[1] G. Rudstam, K. Aleklett, and L. Sihver, At. Data Nucl. Data Tables **53**, 1 (1993).
[2] B. Pfeiffer, K.-L. Kratz, and P. Möller, Prog. Nucl. Energy **41**, 39 (2002).
[3] G. Audi, F. Kondev, M. Wang, B. Pfeiffer, X. Sun, J. Blachot, and M. MacCormick, Chin. Phys. C **36**, 1157 (2012).
[4] G. Audi, F. Kondev, M. Wang, W. Huang, and S. Naimi, Chin. Phys. C **41**, 030001 (2017).
[5] L. A. V. Kogan, Sov. Phys. JETP **5**, 365 (1957).
[6] G. Stetter, Nucl. Sci. Abstr. **16**, 1409 (1962).
[7] E. Burbidge, G. Burbidge, W. Fowler, and F. Hoyle, Rev. Mod. Phys. **29**, 547 (1957).
[8] A. Arcones and G. Martínez-Pinedo, Phys. Rev. C **83**, 045809 (2011).
[9] M. Mumpower, R. Surman, G. McLaughlin, and A. Aprahamian, Prog. Part. Nucl. Phys. **86**, 86 (2016).
[10] R. Surman, M. Mumpower, J. Cass, I. Bentley, A. Aprahamian, and G. C. McLaughlin, in *EPJ Web of Conferences* (EDP Sciences, 2014), Vol. 66, p. 07024.
[11] H. Ohm *et al.*, Z. Phys. A: At. Nucl. **296**, 23 (1980).
[12] K.-L. Kratz, A. Schröder, H. Ohm, G. Jung, B. Pfeiffer, and F. Schussler, Phys. Lett. B **103**, 305 (1981).
[13] K.-L. Kratz *et al.*, Z. Phys. A: At. Nucl. **306**, 239 (1982).
[14] H. Gabelmann *et al.*, Z. Phys. A: At. Nucl. **308**, 359 (1982).
[15] J. Wang, P. Dendooven, M. Hannawald, A. Honkanen, M. Huhta, A. Jokinen, K.-L. Kratz, G. Lhersonneau, M. Oinonen, H. Penttilä *et al.*, Phys. Lett. B **454**, 1 (1999).
[16] F. Montes, A. Estrade, P. Hosmer, S. Liddick, P. Mantica, A. Morton, W. Mueller, M. Ouellette, E. Pellegrini, P. Santi *et al.*, Phys. Rev. C **73**, 035801 (2006).
[17] J. Pereira, S. Hennrich, A. Aprahamian, O. Arndt, A. Becerril, T. Elliot, A. Estrade, D. Galaviz, R. Kessler, K.-L. Kratz *et al.*, Phys. Rev. C **79**, 035806 (2009).
[18] A. Morales, J. Benlliure, T. Kurtukián-Nieto, K.-H. Schmidt, S. Verma, P. Regan, Z. Podolyák, M. Górska, S. Pietri, R. Kumar *et al.*, Phys. Rev. Lett. **113**, 022702 (2014).
[19] R. Caballero-Folch, C. Domingo-Pardo, J. Agramunt *et al.*, Phys. Rev. Lett. **117**, 012501 (2016).
[20] H. Geissel, P. Armbruster, K. Behr, A. Brünle, K. Burkard, M. Chen, H. Folger, B. Franczak, H. Keller, O. Klepper *et al.*, Nucl. Instrum. Methods Phys. Res., Sect. B **70**, 286 (1992).
[21] R. Janik, A. Prochazka, B. Sitar, P. Strmen, I. Szarka, H. Geissel, K.-H. Behr, C. Karagiannis, C. Nociforo, H. Weick *et al.*, Nucl. Instrum. Methods Phys. Res., Sect. A **640**, 54 (2011).
[22] R. Schneider and A. Stolz, *Technical Manual Ionization Chamber MUSIC80*, Tech. Rep. (Technische Universität München, 2000).
[23] A. Morales, Ph.D. thesis, Universidade de Santiago de Compostela, 2011 (unpublished).
[24] E. Casarejos-Ruiz, Ph.D. thesis, Universidade de Santiago de Compostela, 2001 (unpublished).
[25] F. Farinon, Ph.D. thesis, Justus-Liebig-Universität, Gieß, 2011, (unpublished).
[26] J. Kurcewicz, F. Farinon, H. Geissel, S. Pietri, C. Nociforo, A. Prochazka, H. Weick, J. Winfield, A. Estradé, P. Allegro *et al.*, Phys. Lett. B **717**, 371 (2012).
[27] R. Caballero-Folch, Ph.D. thesis, Universitat Politècnica de Catalunya, 2015 (unpublished).
[28] F. Kondev, Nucl. Data Sheets **101**, 521 (2004).
[29] H. Alvarez-Pol, J. Benlliure, E. Casarejos, L. Audouin, D. Cortina-Gil, T. Enqvist, B. Fernández-Domínguez, A. Junghans, B. Jurado, P. Napolitani *et al.*, Phys. Rev. C **82**, 041602 (2010).
[30] L. Chen, W. Plass, H. Geissel, R. Knöbel, C. Kozhuharov, Y. A. Litvinov, Z. Patyk, C. Scheidenberger, K. Siegień-Iwaniuk, B. Sun *et al.*, Phys. Lett. B **691**, 234 (2010).
[31] C. Hinke, M. Böhmer, P. Boutachkov, T. Faestermann, H. Geissel, J. Gerl, R. Gernhäuser, M. Górska, A. Gottardo, H. Grawe *et al.*, Nature (London) **486**, 341 (2012).
[32] K. Steiger, Ph.D. thesis, Technische Universität München, 2009 (unpublished).

[33] C. B. Hinke, Ph.D. thesis, Technische Universität München, 2010 (unpublished).
[34] K. Smith, Ph.D. thesis, University of Notre Dame, 2014 (unpublished).
[35] F. Kondev, Nucl. Data Sheets **109**, 1527 (2008).
[36] F. Kondev and S. Lalkovski, Nucl. Data Sheets **112**, 707 (2011).
[37] S.-C. Wu, Nucl. Data Sheets **110**, 681 (2009).
[38] M. Martin, Nucl. Data Sheets **108**, 1583 (2007).
[39] B. Singh, G. Mukherjee, D. Abriola, S. Basu, P. Demetriou, A. Jain, S. Kumar, S. Singh, and J. Tuli, Nucl. Data Sheets **114**, 2023 (2013).
[40] S.-C. Wu, Nucl. Data Sheets **108**, 1057 (2007).
[41] M. Basunia, Nucl. Data Sheets **108**, 633 (2007).
[42] E. Browne, Nucl. Data Sheets **104**, 427 (2005).
[43] B. Singh, D. Abriola, C. Baglin, V. Demetriou, T. Johnson, E. McCutchan, G. Mukherjee, S. Singh, A. Sonzogni, and J. Tuli, Nucl. Data Sheets **114**, 661 (2013).
[44] M. Basunia, Nucl. Data Sheets **121**, 561 (2014).
[45] J. Chen and F. Kondev, Nucl. Data Sheets **126**, 373 (2015).
[46] M. Gómez-Hornillos, J. Rissanen, J. Taín, A. Algora, K. Kratz, G. Lhersonneau, B. Pfeiffer, J. Agramunt, D. Cano-Ott, V. Gorlychev, R. Caballero-Folch, T. Martínez, L. Achouri, F. Calvino, G. Cortès, T. Eronen, A. García, M. Parlog, Z. Podolyak, C. Pretel, and E. Valencia, Hyperfine Interact. **223**, 185 (2014).
[47] J. Agramunt, A. Garcia, A. Algora, J. Äystö, R. Caballero-Folch, F. Calvino, D. Cano-Ott, G. Cortes, C. Domingo-Pardo, T. Eronen *et al.*, Nucl. Data Sheets **120**, 74 (2014).
[48] V. Gorlychev, Ph.D. thesis, Universitat Politècnica de Catalunya, 2014 (unpublished).
[49] A. Torner, J. Agramunt, A. Algora, L. Batet, R. Caballero-Folch, F. Calviño, D. Cano-Ott, A. García, G. Cortés, I. Dillmann, C. Domingo-Pardo, M. Gómez-Hornillos, V. Gorlychev, M. Marta, T. Martínez, A. Poch, C. Pretel, A. Riego, and J. Taín, *Technical Design Report of the Beta-Delayed Neutron Detector (BELEN) for NUSTAR (DESPEC)*, Tech. Rep. (Universitat Politècnica de Catalunya, Barcelona, 2014).
[50] A. Riego, Ph.D. thesis, Universitat Politècnica de Catalunya, 2016 (unpublished).
[51] S. Agostinelli, J. Allison, K. Amako, J. Apostolakis, H. Araujo, P. Arce, M. Asai, D. Axen, S. Banerjee, G. Barrand *et al.*, Nucl. Instrum. Methods Phys. Res., Sect. A **506**, 250 (2003).
[52] D. B. Pelowitz *et al.*, *MCNPX Users Manual Version 2.5.0*, Tech. Rep. (Los Alamos National Laboratory, 2005).
[53] G. Fishman, *Monte Carlo Concepts, Algorithms and Applications* (1996).
[54] R. Y. Rubinstein and D. P. Kroese, Simulation and the Monte Carlo Method (1981).
[55] G. Audi, M. Wang, A. Wapstra, F. Kondev, M. MacCormick, X. Xu, and B. Pfeiffer, Chin. Phys. C **36**, 1287 (2012).
[56] M. Wang, G. Audi, A. Wapstra, F. Kondev, M. MacCormick, X. Xu, and B. Pfeiffer, Chin. Phys. C **36**, 1603 (2012).
[57] H. N.Kurz, *GSI Data Acquisition System MBS, Release Notes v5.1* (2010).
[58] J. Agramunt, J. Tain, M. Gómez-Hornillos, A. Garcia, F. Albiol, A. Algora, R. Caballero-Folch, F. Calviño, D. Cano-Ott, G. Cortés *et al.*, Nucl. Instrum. Methods Phys. Res., Sect. A **807**, 69 (2016).
[59] http://www.struck.de/sis3302.htm
[60] H. Bateman, Proc. Cambridge Philos. Soc. **15**, 423 (1910).
[61] M. Bernas, P. Armbruster, J. Bocquet, R. Brissot, H. Faust, C. Kozhuharov, and J. Sida, Z. Phys. A **336**, 41 (1990).
[62] J. G. Proakis, M. Salehi, N. Zhou, and X. Li, *Communication Systems Engineering* (Prentice-Hall, Englewood Cliffs, 1994), Vol. 1.
[63] A. Gelman, J. B. Carlin, H. S. Stern, and D. B. Rubin, *Bayesian Data Analysis* (Taylor & Francis, 2014), Vol. 2.
[64] Brookhaven National Laboratory, USA, http://www.nndc.bnl.gov/nudat2/indx_dec.jsp.
[65] A. Morales, G. Benzoni, A. Gottardo, J. Valiente-Dobón, N. Blasi, A. Bracco, F. Camera, F. Crespi, A. Corsi, S. Leoni *et al.*, Phys. Rev. C **89**, 014324 (2014).
[66] D. Fink, T. Cocolios, A. Andreyev, S. Antalic, A. Barzakh, B. Bastin, D. Fedorov, V. Fedosseev, K. Flanagan, L. Ghys *et al.*, Phys. Rev. X **5**, 011018 (2015).
[67] P. Möller, B. Pfeiffer, and K.-L. Kratz, Phys. Rev. C **67**, 055802 (2003).
[68] I. Borzov, Nucl. Phys. A **777**, 645 (2006).
[69] H. Koura, T. Tachibana, M. Uno, and M. Yamada, Prog. Theor. Phys. **113**, 305 (2005).
[70] T. Marketin, L. Huther, and G. Martínez-Pinedo, Phys. Rev. C **93**, 025805 (2016).
[71] I. N. Borzov (private communication).
[72] M. Mumpower, T. Kawano, and P. Möller, Phys. Rev. C **94**, 064317 (2016).
[73] D. Craig and H. Taylor, J. Phys. G: Nucl. Phys. **10**, 1133 (1984).
[74] A. Pakkanen, T. Komppa, and H. Helppi, Nucl. Phys. A **184**, 157 (1972).
[75] C. Wennemann, W.-D. Schmidt-Ott, T. Hild, K. Krumbholz, V. Kunze, F. Meissner, H. Keller, R. Kirchner, and E. Roeckl, Z. Phys. A: Hadrons Nucl. **347**, 185 (1994).
[76] A. Morales, G. Benzoni, N. Al-Dahan, S. Vergani, Z. Podolyák, P. Regan, T. Swan, J. Valiente-Dobón, A. Bracco, P. Boutachkov *et al.*, Europhys. Lett. **111**, 52001 (2015).
[77] Z. Li, Z. Jinhua, Z. Jiwen, W. Jicheng, Q. Zhi, Y. Youngfeng, Z. Chun, J. Genming, G. Guanghui, D. Yifei *et al.*, Phys. Rev. C **58**, 156 (1998).
[78] G. Benzoni, A. Morales, J. Valiente-Dobón, A. Gottardo, A. Bracco, F. Camera, F. Crespi, A. Corsi, S. Leoni, B. Million *et al.*, Phys. Lett. B **715**, 293 (2012).
[79] H. Sagawa, A. Arima, and O. Scholten, Nucl. Phys. A **474**, 155 (1987).
[80] P. Goddard, P. D. Stevenson, and A. Rios, Phys. Rev. Lett. **110**, 032503 (2013).
[81] H. Nakada, Phys. Rev. C **92**, 044307 (2015).
[82] A. Gottardo, J. Valiente-Dobón, G. Benzoni, R. Nicolini, A. Gadea, S. Lunardi, P. Boutachkov, A. Bruce, M. Górska, J. Grebosz *et al.*, Phys. Rev. Lett. **109**, 162502 (2012).
[83] Zs. Podolyák (private communication).
[84] T. Kurtukian-Nieto, J. Benlliure, and K.-H. Schmidt, Nucl. Instrum. Methods Phys. Res., Sect. A **589**, 472 (2008).